Article

Ovarian cancer cells exhibit diverse migration strategies on stiff collagenous substrata

Madhumitha Suresh[1] and Ramray Bhat[1,2,*]

[1]Department of Bioengineering, Indian Institute of Science, Bengaluru, India and [2]Department of Developmental Biology and Genetics, Indian Institute of Science, Bengaluru, India

ABSTRACT   In homoeostasis, the shape and sessility of untransformed epithelial cells are intricately linked together. Variations of this relationship in migrating cancer cells as they encounter different microenvironments are as yet ill understood. Here, we explore the interdependency of such traits in two morphologically distinct invasive ovarian cancer cell lines (OVCAR-3 and SK-OV-3) under mechanically variant contexts. We first established a metric toolkit that assessed traits associated with cell motion and shape, and rigorously measured their dynamical variation across trajectories of migration using a Shannon entropic distribution. Two stiffness conditions on polymerized collagen I with Young's moduli of 0.5 kPa (soft) and 20 kPa (stiff) were chosen. Both the epithelioid OVCAR-3 and mesenchymal SK-OV-3 cells on soft substrata exhibited slow and undirected migration. On stiff substrata, SK-OV-3 showed faster persistent directed motion. Surprisingly, OVCAR-3 cells on stiffer substrata moved even faster than SK-OV-3 cells but showed a distinct angular motion. The polarity of SK-OV-3 cells on stiff substrata was well correlated with their movement, whereas, for OVCAR-3, we observed an unusual "slip" behavior, wherein the axes of cell shape and movement were poorly correlated. Whereas SK-OV-3 and OVCAR-3 showed greater mean deformation on stiffer substrata, the latter was anticorrelated with variation in angular motion or the mean deviation between shape and motility axis for SK-OV-3 but poorly correlated for OVCAR-3. Moreover, on softer substrata OVCAR-3 and SK-OV-3 were relatively rigid but showed greater shape variation (with OVCAR-3 showing a higher fold change) on stiffer substrata. Our findings suggest that greater deformability on stiffer milieu allow epithelioid cells to overcome constraints on the congruence in axis of shape and motion seen for mesenchymal cells and display distinct motile behaviors across this phenotypic spectrum.

SIGNIFICANCE   We compared the speed and shape of migratory epithelioid (OVCAR-3) and mesenchymal (SK-OV-3) ovarian cancer lines on soft and stiff collagen I gels. On stiff gels, SK-OV-3 cells showed higher speed, more persistent migration, better shape-motility alignment, and higher deformability. The higher the mean deformation, the greater was the persistence and better the shape-motion alignment. Remarkably, on stiffer gels, OVCAR-3 cells moved even faster, but showed angular motion, poor shape-motility alignment, and higher deformation; however, the deformation was uncorrelated with persistence or shape-motion alignment. Our work offers a rigorous methodological toolkit to study motile cell behavior but also reveals surprising morphomigratory traits of transformed epithelioid OVCAR-3 cells that may underlie the aggression of high-grade serous ovarian cancer.

INTRODUCTION

Cell migration is an essential phenomenon in organogenesis, homeostasis, wound healing, and immunosurveillance (1). It involves a continuous coordination between physicochemical cues external to the cell and its internal signaling cascades through active cytoskeletal rearrangement (2,3). Abnormal migratory behaviors due to aberrant signaling or changes in the external microenvironment, in turn, have been shown to be strongly associated with histopathological states such as cancer, which is typified by ectopic localization of cells due to their invasion outside native niches: a process referred to as metastasis (4,5). Such changes in the microenvironment have also been seen to have a broad effect on cellular morphology. A well-known correlation between morphology and migration is seen when polygonal epithelial cells transit to a dysmorphic "mesenchymal" state with a concomitant increase in motility (epithelial-to-mesenchymal transition) (6). Recent studies also show that cancer cells adopt an ameboid transition state by reducing

cell-cell and cell-extracellular matrix (ECM) adhesion and further increase their rate of migration. This constant switch between epithelial to mesenchymal and ameboid phenotypes has been postulated to play a major role in cancer cell survival and metastasis (7,8). Current studies have highlighted the importance of measuring cell morphological features as they help indicate the physiological status of a cell and distinguish cancer cells from their untransformed counterparts (9,10). The most common mathematical metrics used currently for quantifying cellular shape include aspect ratio, eccentricity, shape index, and circularity, while for cell migration, it includes accumulated distance, average speed, turning angles, and mean-square displacement (MSD) (11,12).

Shannon entropy, which denotes the information contained in a variable, has been increasingly used in biological systems for investigating diversity and patterns in ecology, characterizing periodicity in genomic and transcriptomic data, and identifying cancer tissue samples, as well as for identifying potential therapeutic targets (13–16). Recent studies by Liu and co-workers have also shown the significance of Shannon entropy as a measure in extracting the time-variant dynamics of cellular migration and morphology (17–19). Advancement in computational approaches has resulted in several machine learning and neural network-based approaches for cellular segmentation and classification models for distinguishing and characterizing various morphology and migratory modes (20–22). However, the complexity of such models has drawn researchers back to using static mathematical parameters to quantify morphology and migration, necessitating efforts to come up with more creative combinations or toolkits of metrics that describe motility behavior across time and space. Furthermore, as studies look into the characteristics of morphology and migration of cells as separate entities, there is a need to rigorously investigate how correlated these processes are under different microenvironmental contexts (21,23) (see a recent study by Kołodziej et al., which provides fresh insights on the interdependency between both metrics using numerical parameters that incorporate cell geometry, cell orientation, and their corresponding migratory behavior (24)).

The need for decoding cellular morphomigratory dynamics is particularly relevant to invasive cancer cells, which exhibit distinct morphological features and migratory characteristics. This study focuses specifically on epithelial ovarian cancer, which ranks as the seventh most common cancer in terms of incidence in women as well as the eighth most common cause of death from cancer in women (25). It uses one cell line each representing high-grade serous ovarian cancer and nonserous cancer. Although having distinct histopathological features, both cells are known to metastasize in animal models (26).

The ability of cancer cells to metastasize rapidly comes from their ability to change their surrounding microenvironment as well as to adapt to such altering niches (27). Bio-

physical cues from the ECM microenvironment include stiffness, porosity, and topography of the underlying substrate (28,29). Ovarian cancer progression involves cells navigating transcoelomic tissues such as lymph nodes, peritoneal linings, and fibrosed areas that show a range of stiffness from 0.5 to 25 kPa. Hence, in this study, we investigate the role of substrate stiffness using collagen-coated polyacrylamide hydrogels mimicking normal (soft, 0.5 kPa) and tumor (stiff, 20 kPa) tissue on the spatiotemporal cellular plasticity in ovarian cancer cells. While the motility of transformed mesenchymal cells and that of untransformed epithelial sheets have received extensive attention, behaviors of epithelioid cancer cells within, or on the surface of, ECM are as yet ill understood.

In this study, we develop a toolkit to rigorously analyze parameters relating to migration and morphology of cancer cells. We then utilize the toolkit to study the role of biophysical cues on ovarian cancer cells' phenotype over a short but finely sampled spatiotemporal scale. Our study reveals surprising effects of the mechanical microenvironment on the locomotive plasticity of ovarian cancer cells.

MATERIALS AND METHODS

Cell culture and time-lapse setup

This study used two different ovarian cancer cell types—OVCAR-3 and SK-OV-3 (a kind gift from Professor Rajan R. Dighe, Indian Institute of Science.). The OVCAR3 cells were cultured in RPMI medium supplemented with 20% FBS (Gibco, Waltham, Massachusetts), while SK-OV-3 cells (WT and GFP-labeled) were cultured in McCoy's medium supplemented with 10% FBS. Approximately 12,000 cells were seeded per well in an 8-well chamber slide coated with the required substrate. Cells were then kept in a cell incubator with 5% CO_2 at 37°C and humidification for overnight adhesion. The main objective was to obtain sparsely distributed cells to collect single-cell data. Time-lapse experiments were performed on an inverted epifluorescence microscope (IX83 Olympus, Tokyo, Japan) at 20× objective for 3 h. Since, cellular protrusion dynamics are in the range of 120–180 s, snapshots are taken at a time interval of 2 min (30,31).

Polyacrylamide gel preparation

Polyacrylamide gels of required stiffness were prepared in reference to the relative concentrations stated in Tse and Engler (32).

Activation of glass slide

Activation of glass slides (8-well chamber slides) was performed using 10% (3-aminopropyl) trioethoxysilane with an incubation time of 20 mins. Excess silane was removed by washing twice with autoclaved filtered water. Fixation was then done using 0.5% glutaraldehyde for 45 min. Excess glutaraldehyde was removed by washing thrice with autoclaved filtered water.

Preparation of sandwich coverslip

The sandwich coverslip was coated with Rain-X to provide a hydrophobic coating. After 10 min, the excess coating was removed by rinsing twice with autoclaved filtered water.

Preparation of hydrogel(s)

A solution of acrylamide and bis-acrylamide of the required concentration for specific stiffness was prepared in autoclaved filtered water. For 0.5 kPa, 0.75 mL of 40% acrylamide and 0.3 mL of 2% bis-acrylamide were mixed in 8.95 mL of autoclaved filtered water. For 20 kPa, 2 mL of 40% acrylamide and 1.32 mL of 2% bis-acrylamide were mixed in 6.68 mL of autoclaved filtered water. Polymerizing gel solution (60–80 μL) is usually added per well. Therefore, to the required volume of acrylamide and bis-acrylamide solution, 1/100th of the total volume of 10% ammonium persulfate and 1/1000th of the total volume of tetramethylethylenediamine were added to produce the polymerizing gel. This polymerizing gel was immediately added to the activated glass slide. The hydrophobic sandwich coverslip was placed immediately on top of the solution to uniformly spread the gel in the glass slide. The coverslip is usually removed within 5 mins, as the gel usually forms by that time.

ECM coating the gel surface

The gel is initially coated with sulfo-SANPAH, a heterobifunctional protein cross-linker for ECM coating. Since sulfo-SANPAH is a photoreactive cross-linker, the coated gel is exposed to UV for 25 mins. The gel is then washed with phosphate-buffered saline (PBS) thrice to remove excess sulfo-SANPAH. To the activated gels, 100 μg/mL of collagen was added. An initial collagen (Gibco) concentration of 1 mg/mL was prepared. Initial precooling of all the gel components (type I collagen, $10\times$ DMEM, 2 N NaOH, PBS) and an Eppendorf tube were done. To prepare a volume of 100 μL of 1 mg/mL collagen, 33.3 μL collagen of stock concentration 3 mg/mL was neutralized with 0.67 μL of 2 N NaOH. The solutions were thoroughly mixed until a pink color was observed. To this, 10 μL of $10\times$ DMEM and 56 μL of PBS were added. This was further diluted to 100 μg/mL by the addition of PBS. The solutions were thoroughly mixed, and a volume of 100 μL was added to each well within an 8-well chamber. The 8-well chambers are kept in the incubator at 37°C for 45–60 mins for fast polymerization and then transferred into the refrigerator at 4°C overnight to enhance the duration for attachment of collagen protein to the gel surface. The well chambers are again placed in the incubator 1 h before seeding cells for the experiment.

Image processing and analysis

Segmentation, binarization, and analysis

The image processing was done in an open-source package, namely, Fiji (33). The raw time-lapse image sequence was converted to .tif format and cropped to obtain fields with a higher number of single cells. To segment the fluorescently labeled cells (GFP labeled) from each frame, an initial adjustment of brightness and contrast was made to get a clear outline of the body of the cell using Fiji. This was followed by default thresholding to obtain binarized images. To the obtained processed file, a fitted ellipse was overlaid to get the required parameters using an ImageJ Macro code. Cell measurements such as centroid, major axis length, minor axis length, major axis angle, area, and perimeter were then generated using the "Analyze particles" option within Fiji. Sorting of each cell from the generated excel sheet of parameters was done manually. Time-lapse trajectories were taken in a manner to avoid instances of cells colliding with or adhering to each other or dividing into two daughter cells.

Quantitative descriptors of cell shape and migration within the toolbox

From the above parameters, the required metrics within the toolbox was constructed as indicated in Fig. 1. The displacement vector for each frame was calculated by the distance traveled by the centroid from preceding (n–1) frame to current (n) frame. Global turning angle (GTA) (θ) was calculated as the angle made by displacement vector with the x axis, and given by the formula $\tan^{-1}\left(\frac{y_{i+1}-y_i}{x_{i+1}-x_i}\right)$. GTA values have a range between -180 and $180°$. Relative turning angle (RTA) (α) was calculated between current displacement vector (between n–1 and n frames) and successive displacement vector (between n and n+1 frames), given by the formula $\cos^{-1}\left(\frac{d_i\,d_{(i+1)}}{|d_i|*|d_{(i+1)}|}\right)$, where d_i denotes displacement vector. This angle calculates the smallest positive angle between two vectors, which is always between 0 and 180°. This is because $\cos(\alpha)$ returns value in the range [–1,1] and inverse cosine (arccos) returns angle in the range [0,180]. Given that, in this study, we focus on single-cell migration we have not distinguished between, clock- or counterclockwise turn. Major axis (MA) endpoints were calculated from the length and centroid values generated before. The morphomigratory angle (μ) was obtained by calculating the acute angle between major axis and the successive displacement vector (between n and n + 1 frames). The MA dynamics (Φ) was obtained by calculating the difference in MA angle (generated earlier) in current and preceding frames. It is to be noted that values of Φ are not considered as plausible indicators of orientation in the case of rounded cells due to anomalies in major axis determination. Elongation (ε) was calculated by the ratio of minor axis length to major axis length. The persistence ratio was calculated as the ratio between Euclidean distance and accumulated distance. For detailed entropy calculation protocol please see Data S1. For bin number measurement, we applied three rules: Cencov's rule and Terrell and Scott's rule predicted the optimal bin number to be ~5, whereas Rice's rule predicted an optimal number to be 9 (34). We have used 5 bins for all the calculations in this paper and, in fact, observe that, for the first data set, changing the number to 9 leaves the inferences unchanged (Data S1). Furthermore, MSD was calculated using the formula $\text{MSD}(\tau) = \frac{1}{T-\tau+1}\sum_{i=0}^{T-\tau}\left[(x_{(i+\tau)} - x_i)^2 + (y_{(i+\tau)} - y_i)^2\right]$, where $\text{MSD}(\tau)$ represents the MSD for a single cell with step size τ in a total time of T. Since, the frame acquisition rate was every 2 min, step size was increased in increments of 2 up to 60. To obtain a population average for each step size, MSDs were averaged over all cells. Log of average MSD and step size was calculated and plotted to fit a linear regression curve and obtain the slope value (k). Similarly, root mean-square (RMS) of turning angle and elongation metrics was calculated with an additional square root calculation of the mean-squared values. All the parameters were calculated using MATLAB version 23.2.0.2428915 (R2023b) update 4.

Statistical analysis

All time-lapse experiments were performed thrice or more (mentioned otherwise). GraphPad Prism 8.0.1 was used for generating graphs and statistical analysis. For statistical analysis, one-way ANOVA was performed. The correlation matrix (seen in Fig. 5, *E* and *F*) is performed using a corrplot package in R, based on Pearson's correlation coefficient, between all biological replicates, after which the average of the values is considered. The total number of cells analyzed in each condition are as follows: SK-OV-3 (0.5 kPa), 172; SK-OV-3 (20 kPa), 175; OVCAR-3 (0.5 kPa), 140; OVCAR-3 (20 kPa), 135. The ImageJ Macro and MATLAB codes used in the above study are available in the following github link: https://github.com/madhumitha-rsuresh/Morphomigratory-parameters.

RESULTS

Integration of a morphomigration toolkit with entropic measurements reveals distinct modes of migration

The metrics we have calculated in the context of invasive ovarian cancer cells in this manuscript were chosen to
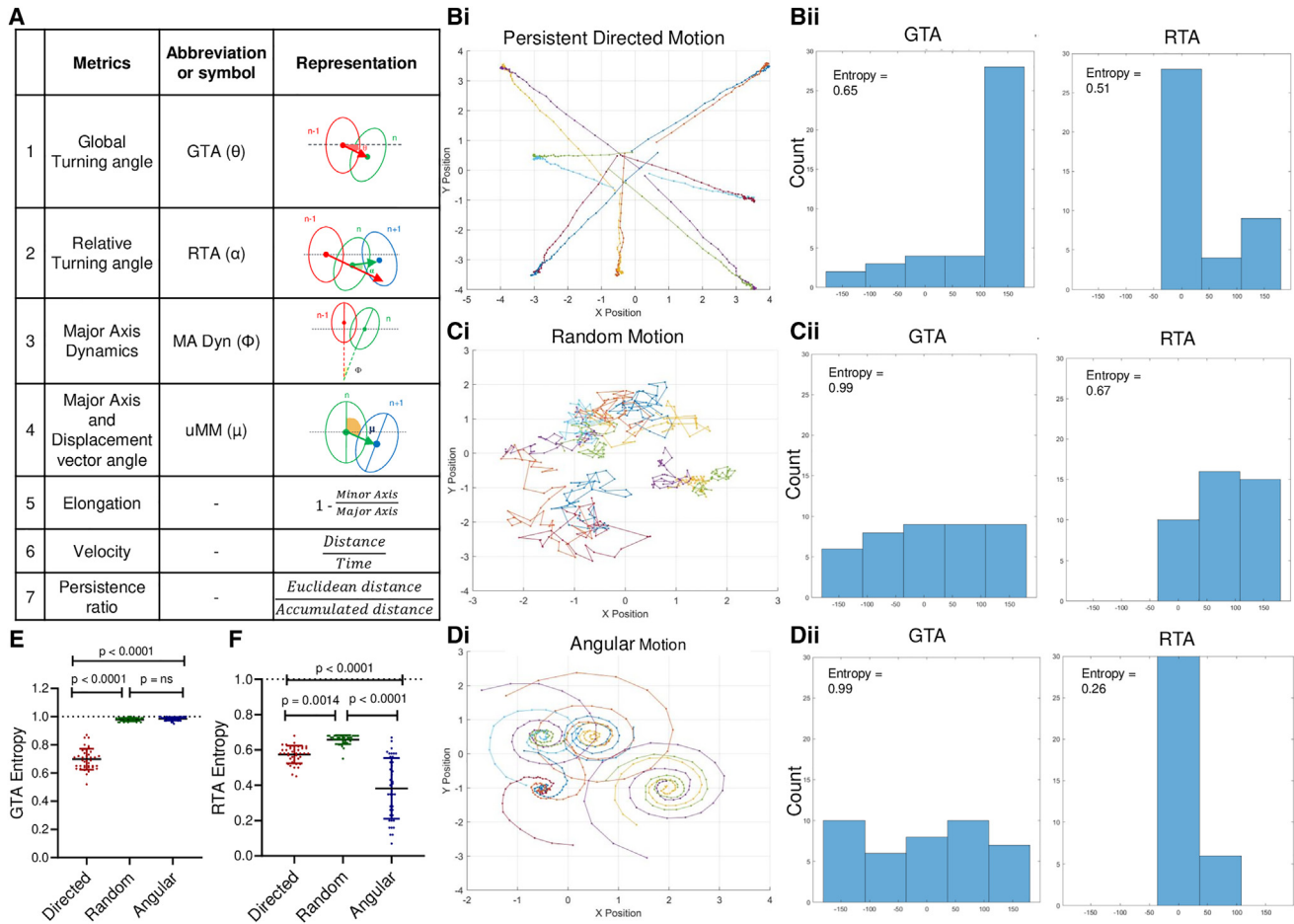
FIGURE 1 Metrics for the study of morphological and migrational features of cancer cells (*A*) Toolkit with the corresponding abbreviation, formula, and graphical representation. (*B–Di*) Synthetic tracks generated using discretized and modified Ornstein-Uhlenbeck equation corresponding to persistent directed motion (*Bi*), random motion (*Ci*), and angular motion (*Di*). (*B–Dii*) Histograms corresponding to turning angle distribution (GTA and RTA), which is used for entropy calculation. (*E*) Comparative analysis of mean entropy of global turning angle for each migratory mode. (*F*) Comparative analysis of mean entropy of relative turning angle for each migratory mode (n = 40; statistical analysis was performed using one-way ANOVA).

estimate cell motility, shape, orientation, and derive their correlations with their migratory direction. These metrics and their representative formulae or pictorial representations are shown in Fig. 1 *A*. To elucidate the 'uncertainty' in cellular state change over time, Shannon entropy (H) was used to decode the metric flux. Shannon entropy (H) was calculated using the formula,

$$ H = - \sum_{i=1}^{n} p_i \, log_2(p_i) $$

where n represents the total number of events and p_i represents the probability for each event (35). Using this definition, entropy for each metric within an individual cell was calculated by sorting every metric value within the given time frame into specific ranged bins and measuring the probability for each bin. Here, n represents number of bins and p represents the probability of a given metric found within the bin at specific time point. Hence, this gives us a

clear histogram depicting the probability distribution of the corresponding metric values within the bins. Furthermore, the entropy values were normalized with the maximum possible entropy (H), which corresponds to equal probability occurrence in all bins, to obtain a dimensionless quantity from 0 to 1 for easier comparison between different scenarios. The Shannon entropy used here goes with the conventional Gibb's entropy interpretation that an entropic value closer to unity corresponds to "highly random" dynamics, while a value closer to "0" corresponds to "ordered dynamics."

To test the sensitivity of the toolkit, synthetic data corresponding to specific migratory modes were generated using a modified Ornstein-Uhlenbeck equation (36) involving drift, diffusion, and an additional rotational term in MATLAB.

$$ dX(t) = - \theta(X(t) - \mu_x)dt + \sigma dW_x(t) + \omega(Y(t) - \mu_y)dt $$

$$dY(t) = -\theta(Y(t) - \mu_y)dt + \sigma dW_y(t) - \omega(X(t) - \mu_x)dt$$

Here, θ denotes the rate of reversion to the mean; μ is the mean position; σ denotes the volatility of the process (corresponds to random fluctuation intensity); ω denotes rotational frequency; dW_t denotes Wiener process (Brownian motion). X and Y correspond to centroid positions that evolve over time under the above equations. Furthermore, the above equations were discretized for simplification using a constant step size (Δt) of 0.25 for a total time frame of 10 min.

$$X_{i+1} = X_i - \theta(X_i - \mu_x)\Delta t + \sigma\sqrt{\Delta t} \cdot N(0,1) + \omega(Y_i - \mu_y)\Delta t$$

$$Y_{i+1} = Y_i - \theta(Y_i - \mu_y)\Delta t + \sigma\sqrt{\Delta t} \cdot N(0,1) + \omega(X_i - \mu_x)\Delta t$$

Here, $N(0,1)$ denotes a standard normal random variable. Fig. 1, *Bi*, *Ci*, and *Di* denotes three different migratory modes, namely, persistent directed, random, and angular motion, obtained via tuning the values of θ, μ, σ, and ω. The first term, referred to as the drift term, can be altered through higher θ and μ values and is used for directing the cell to a specific faraway point. The second term, referred to as the diffusion term, can be altered via σ value, where the higher the value, the higher the induction of random fluctuation to the system. The final term, referred to as the rotational term, can be altered through the ω value, which is used for inducing angular change to the system. For persistent directed motion, the values of μ were kept three to four coordinates away from the initial point with minimal fluctuation ($\sigma = 0.05$) and null rotational frequency. For random motion, the μ values were kept closer to the initial starting point with a higher fluctuation rate ($\sigma =$ up to 0.5) and null rotational frequency. For angular motion, the values of μ and ω ($\omega =$ up to 1.5) were allowed to vary, but the fluctuation rate was kept minimal ($\sigma = 0.05$).

The synthetic tracks generated using the above equation for different migratory modes are shown in Fig. 1, *B–D*. The variation in entropy values for distinct migratory metrics, specifically global and relative turning angles (GTA and RTA, respectively), clearly indicated the type of migration the particles have undertaken (Fig. 1, *E* and *F*; graph depicting mean entropies of GTA and RTA, respectively, for particles of different migratory modes; statistical analysis is done using one-way ANOVA). While the GTA corresponds to the current direction in which the particle has moved with respect to a fixed axis, the RTA corresponds to the trajectory the particle has taken with respect to its previous position (37). Fig. 1, *E* and *F* show a comparison between the mean entropy for the two metrics for individual trajectories. It was seen that the particles that move in a

persistent directed motion have lower mean GTA and RTA entropy (angle distributions shown in Fig. 1 *Bii*; see Fig. 1, *E* and *F*). In comparison, those having a random/Brownian motion have higher mean GTA and RTA entropy (angle distributions shown in Fig. 1 *Cii*; see Fig. 1, *E* and *F*). In the case of angular motion, a constant small turn results in lower mean RTA entropy, while the mean GTA entropy increases due to a wider directional range (angle distributions shown in Fig. 1 *Dii*; see Fig. 1, *E* and *F*). Hence, the synthetic data confirm the efficacy of the toolkit to differentiate between specific migratory modes based on direction and persistence.

Substrata stiffness influences the rate of migration and persistence of ovarian cancer cells

To compare the impact of the biophysical cues of the substrata matrix microenvironment on the migratory dynamics of ovarian cancer cells, polyacrylamide hydrogels of Young's modulus 0.5 kPa (representing the lower value of stiffness spectra that are indicative of the mechanical heterogeneity of untransformed ovarian tissues with the lowest values at the edge, where the ovarian capsule and the prospective site of tumorigenesis is located), and, addition, also representative of the stiffness of adipose tissues rich in omentum) and 20 kPa (representing the mean stiffness of fibrosed desmoplastic tissues seen across different patterns of high-grade serous ovarian cancers) were used (38,39). Both SK-OV-3, a mesenchymal aggressive cell line, and OVCAR-3, an epithelioid metastatic cell line, when cultivated on soft substrata, moved with a slower speed than those on stiffer substrata (Fig. 2, *A–D*; images represent migration trajectories with a color heatmap representing speed values at different time points; inset of a single trajectory shown on the right). Confirmation of lower mean speed values of low stiffness-cultured cells is also shown in Fig. 2 *E* (graph depicting individual cell speeds on soft and stiff substrata; significance computed using one-way ANOVA). Interestingly, OVCAR-3 cells, known to have greater epithelioid characteristics, were faster than mesenchymal SK-OV-3 cells agnostic of stiffness. Furthermore, the mean entropy for speed was also higher for both cells on stiffer substrata compared with softer substrata, as shown in Fig. 2 *F* (graph depicting mean entropies of cell speed on soft and stiff substrata; significance computed using one-way ANOVA) as well as in Fig. 2, *C* and *D*, where the heatmap reveals motion driven by constant switching between low- and high-speed rates compared with Fig. 2, *A* and *B*.

The substrata-contextual difference in migration speed led us to ask whether OVCAR-3 and SK-OV-3 cells have distinct migration modes, especially in stiffer matrix microenvironments. The possibility of distinct migratory modes was initially characterized by measuring MSD values as a
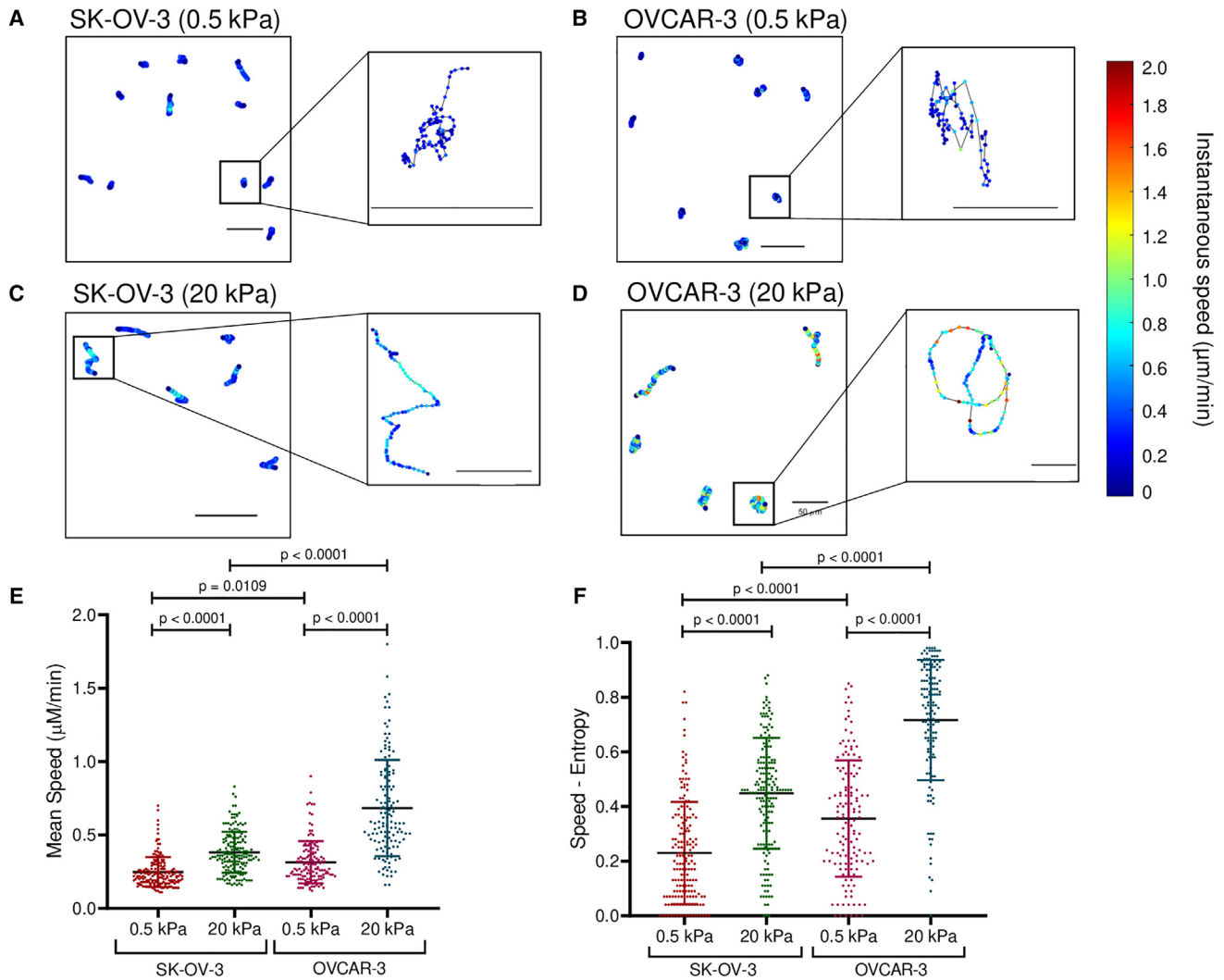
FIGURE 2 Determination of speed parameters of SK-OV-3 and OVCAR-3 cells. (*A–D*) Pictorial representation of cell trajectories of (*A*) SK-OV-3 on low stiffness (0.5 kPa), (*B*) OVCAR-3 on low stiffness, (*C*) SK-OV-3 on high stiffness (20 kPa), and (*D*) OVCAR-3 on high stiffness (20 kPa) with each data point color coded to the corresponding speed value at that particular time point. Inset highlights the trajectory of a specific cell within the field. (*E*) Comparative analysis of mean speed for both the cell types on low and high stiffness. (*F*) Comparative analysis of entropy of speed for both cell types on low and high stiffness (n = 3; statistical analysis was performed using one-way ANOVA). Scale bars, 50 μm and 10 μm (inset).

function of time interval τ, fit into a power law to identify the diffusivity of the system. A constant slope value of k = 1 indicates random motion, while that of k = 2 indicates ballistic motion. Other values, such as those between 0 and 1 indicate subdiffusive motion, while those between 1 and 2 indicate superdiffusive motion (40). Both SK-OV-3 and OVCAR-3 cell types showed superdiffusive motility on low and high stiffness (Fig. 3, *A–D*, where *A* and *B* represent the time-resolved migration of the centroids of representative SK-OV-3 cells on 0.5 and 20 kPa gels, respectively, and *C* and *D* represent the same for OVCAR-3 cells; see also Videos S1, S2, S3, and S4; MSD plots shown in Fig. 3 *E*). However, the migration of OVCAR-3 cells on lower stiffness was more random (k = 1.07) when compared with that on higher stiffness (k = 1.44). SK-OV-3 cells, on

the other hand, showed directed motion in both cases, with increasing stiffness increasing the directionality further (k = 1.58 and 1.78 for 0.5 and 20 kPa gels, respectively). This was further quantified and interpreted through measuring the GTAs and RTAs.

The mean GTA entropy for both cells on lower stiffnesses was high, suggesting lower persistence in motion; on stiffer gels, SK-OV-3 had a lower mean GTA entropy than OVCAR-3, indicating a relatively more persistent migration for the former (Fig. 3 *F*; significance computed using one-way ANOVA). The mean RTA entropy for both cells on lower stiffnesses was also high; on stiffer substrata, whereas the mean RTA entropy of SK-OV-3 was low, this was (in contrast to GTA entropy) also found to be low for OVCAR-3 cells (Fig. 3 *G*; significance
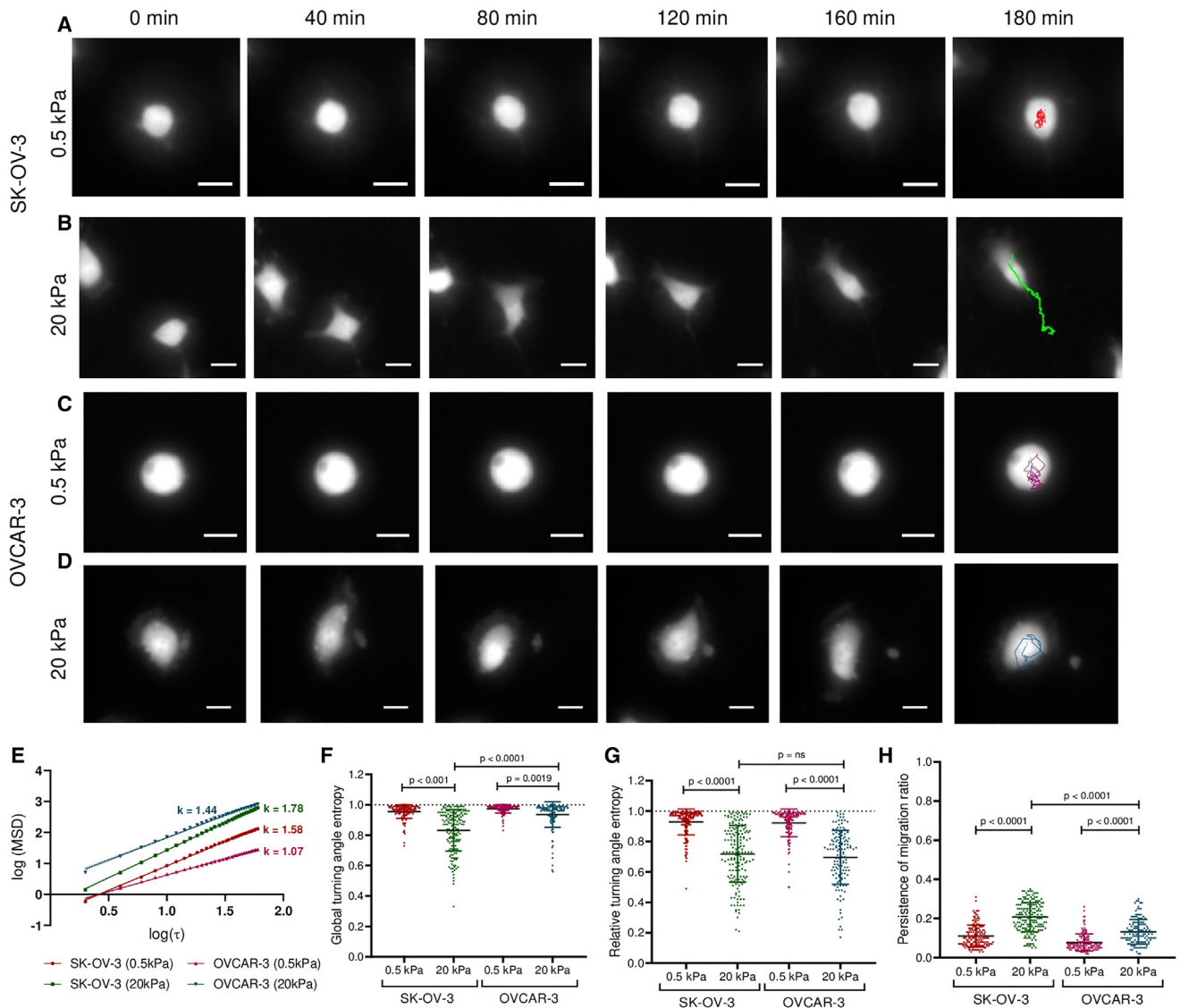
FIGURE 3 Determination of the diffusive nature and angular traits of motion in SK-OV-3 and OVCAR-3 cells. (A–D) Snapshots of time-lapse images at specific time points along with the trajectory for SK-OV-3 on low (A, cell boundary in *red*) and high (B, cell boundary in *green*) stiffness and for OVCAR-3 cells on low (C, cell boundary in *purple*) and high (D, cell boundary in *blue*) stiffness. The time lapses have been performed at 2-min intervals but for visualization, representative 40-min interval images are shown. (E) Comparative analysis of a representative set of the MSD values from the cell tracking data of both cell types on low and high stiffness based on linear regression fit on log-log plot of MSD and t values. Slope value is indicated by k. (F) Comparative analysis of the GTA entropy for both cell types on low and high stiffness. (G) Comparative analysis of the RTA entropy for both cell types on low and high stiffness. (H) Comparative analysis of persistence ratio for both cell types on low and high stiffness (n = 3; statistical analysis was performed using one-way ANOVA). Scale bar, 20 μm. Videos S1, S2, S3, and S4 represent the time-lapse videos of the corresponding snapshots.

computed using one-way ANOVA). Compared with the entropic signatures seen for our synthetic data in Fig. 1 and confirmed through the time lapses, SK-OV-3 on high stiffness migrated in a directed manner, whereas OVCAR-3 on high stiffness showed migration in an angular fashion. This was confirmed through the measurement of persistence ratio in SK-OV-3 cells, which showed higher mean values than for OVCAR-3 cells, with both cells showing greater persistence on stiffer substrata than on softer controls (Fig. 3 H; graph depicting mean persis-

tence ratios on soft and stiff substrata; significance computed using one-way ANOVA). The RMS values of GTA for both cells on both stiffness showed time-invariant behavior (Fig. S1 A). While the RMS values of RTA were invariant for SK-OV-3, for OVCAR-3, especially on high stiffness substrata, there was a marked increase, which can be explained by the increase in relative turn calculated when the timescales for measurement in angular motion are lengthened, consistent with the inferred migratory dynamics seen in Fig. 3.
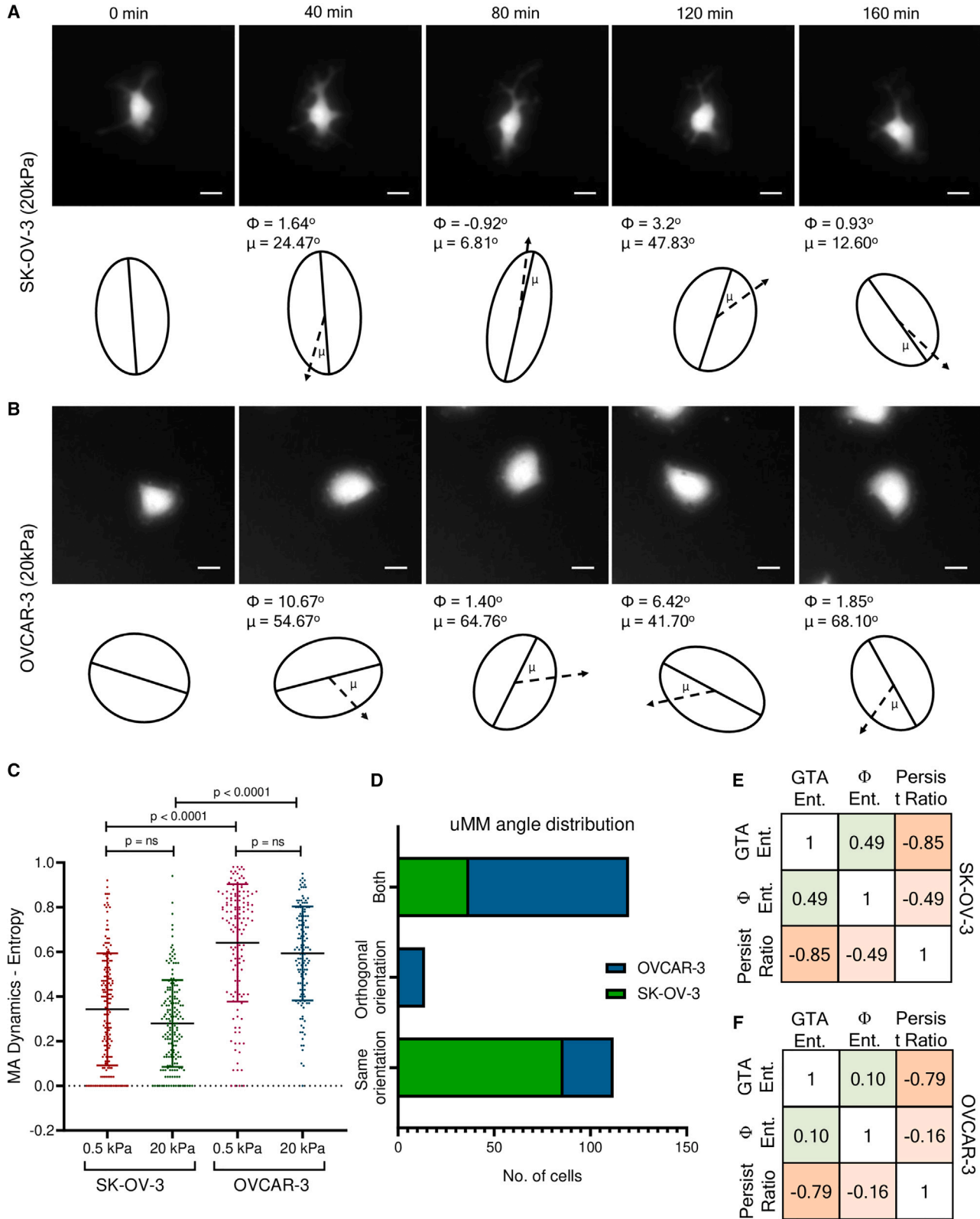
FIGURE 4 Determination of the dynamics of shape axes in SK-OV-3 and OVCAR-3 cells. (*A* and *B*) Snapshots of time-lapse images at specific time points for SK-OV-3 (*A*) and OVCAR-3 (*B*) cells on high stiffness. Corresponding graphical representation of ellipse fit along with their major axis and the angle the latter makes with the axis of motility (denoted as the morphomigrational angle μ) is depicted. MA dynamics (Φ) and morphomigrational angle (μ) are mentioned for the frames (representative snapshots for visualization are taken at time intervals of 40 min; however, the analysis is done for images acquired

(legend continued on next page)

Ovarian cancer cells show morphology-specific correlation between axes of shape and migration on high stiffness

Thus far, our measurements for assessment of migration explored the spatial dynamics of the centroid of cells. To explore associations between the axes of their polar shapes and their motion, the angular change in major axis orientation (denoted by the angle Φ) and the angle between their shape (major axis) and motility axis (or morphomigrational angle denoted by μ) between consecutive time frames was measured over time (see Fig. 4, *A* and *B* for time-resolved representative photomicrographs of SK-OV-3 and OVCAR-3 cells on stiff substrates with major axes; the Φ and μ values are computed across time lapses with 2-min intervals, although, for visualization, cell outlines at every 40-min interval has been shown; see also Videos S5 and S6). For SK-OV-3, the mean Φ entropy was unchanged between soft and rigid substrata with both showing significantly lower values than their OVCAR-3 counterparts (Fig. 4 *C*; graph depicting mean entropies of major axis orientation on soft and stiff substrata; statistical analysis was performed using one-way ANOVA). OVCAR-3 showed higher mean entropy of Φ than SK-OV-3 on soft and stiff substrata, indicating a constant change in orientation during its migration, especially in rigid gels, which could be explained by its angular trajectories indicated in Fig. 3.

To extrapolate this finding and correlate it with orientation and migration, we measured entropy of μ for SK-OV-3 and OVCAR-3 on stiff substrata (Fig. S2 *A*). The mean μ entropy for SK-OV-3 was significantly lower than OVCAR-3, which suggested a variation in the axes of shapes and movement of the latter. Visual examinations under the microscope and in the time-lapse of OVCAR-3 also suggested instances where the movement of cells was often orthogonal to its shape polarity (which we call slip behavior). Therefore, we measured if the μ values for a given cell along its motility trajectory were predominantly (60% or more) below 45° (indicating [near] alignment of shape with motility axes) or above 45° (indicating [near] orthogonal alignment of shape with motility axes). Pie charts for the two cell types indicate that, for SK-OV-3, 70% of cells show trajectories with μ values lesser than 45° in more than 60% of frames, while 30% show trajectories for which equivalent μ values are seen with neither the greater or less than 45° values dominant over the other.

For OVCAR-3, 21% show predominant frames with μ values less than 45°, but 11% also show predominant frames with μ values greater than 45°, signifying a slip behavior (Figs. S2, *B*, *C* and 4 *D* show how, only in OVCAR-3 cells, the slip behavior dominates, whereas an aligned behavior is predominant in SK-OV-3 cells).

A correlation matrix between mean GTA entropy, mean Φ entropy, and mean persistence ratio for both cell types also revealed a relatively greater correlation between migratory direction and orientation dynamics in SK-OV-3 cells (Fig. 4 *E*; correlation $= 0.49$ between entropic values for Φ and GTA entropy) than OVCAR-3 cells (Fig. 4 *F*; correlation $= 0.10$). This gives a new insight into understanding the impact of high stiffness on the migratory capacity of epithelioid cancer cells as they undergo a constant speed and polarity change (often uncorrelated) to push through different directions.

Global deformability of cells increases with an increase in stiffness

We next asked whether ovarian cancer cells on higher stiffness underwent morphological axis alteration through a global shape alteration. To address this, we measured the elongation ratio (see Fig. 5 *A*) from best-fitted ellipse parameters and calculated its distribution to measure elongation entropy values. As seen in Fig. 5, *A–D* (which shows time-resolved shape changes in SK-OV-3 and OVCAR-3 cells grown on softer and stiffer substrata, respectively, with their global cell shapes denoted using distinct colors; see also Videos S7, S8, S9, and S10), both cell types on lower (relative to higher) stiffness were less deformable, suggesting that the cells on soft gels behaved like rigid objects with a rounded morphology, as indicated by lower mean elongation values (Fig. 5 *E*; graph depicting mean values of elongation ratio of cells on soft and stiff substrata; statistical analysis was performed using one-way ANOVA). The RMS values of mean elongation showed time-step invariance (Fig. 5 *F*). On stiffer substrata, SK-OV-3 cells showed anticorrelations between mean elongation values and GTA entropy (-0.51), and also mean μ (-0.61) (Fig. 5 *G*). This indicated that the more elongated the cells were, the lower the deviation in the axes of their shape and migration. Elongation in cellular morphology is a function of the cellular cytoskeletal state, which seems to constrain the migratory behavior of these mesenchymal cells along

---

at 2-min intervals). (*C*) Comparative analysis of MA dynamics entropy for both cell types on low and high stiffness. (*D*) Bar graph depicting the number of SK-OV-3 (*green*) and OVCAR-3 (*dark teal*) cells in whose trajectories, μ values of both greater than or less than 45° are equivalently observed (*top*), in whose trajectories, μ values of greater than 45° are observed for 60% or more of the recorded time points (*middle*), indicating slip motion, and in whose trajectories, μ values of less than 45° are observed for 60% or more of the recorded time points (*bottom*) indicating similar orientation of shape and motion (see also Fig. S2). (*E* and *F*) Correlation matrix between mean entropy value of GTA, mean entropy value of Φ, and the persistence ratio in SK-OV-3 (*E*) and OVCAR-3 (*F*) cells on high stiffness (*green shading* highlights correlation and *orange shading* highlights anticorrelation) (n = 3; statistical analysis was performed using one-way ANOVA). Scale bar, 20 μm. Videos S5 and S6 represent the time-lapse videos of the corresponding snapshots.
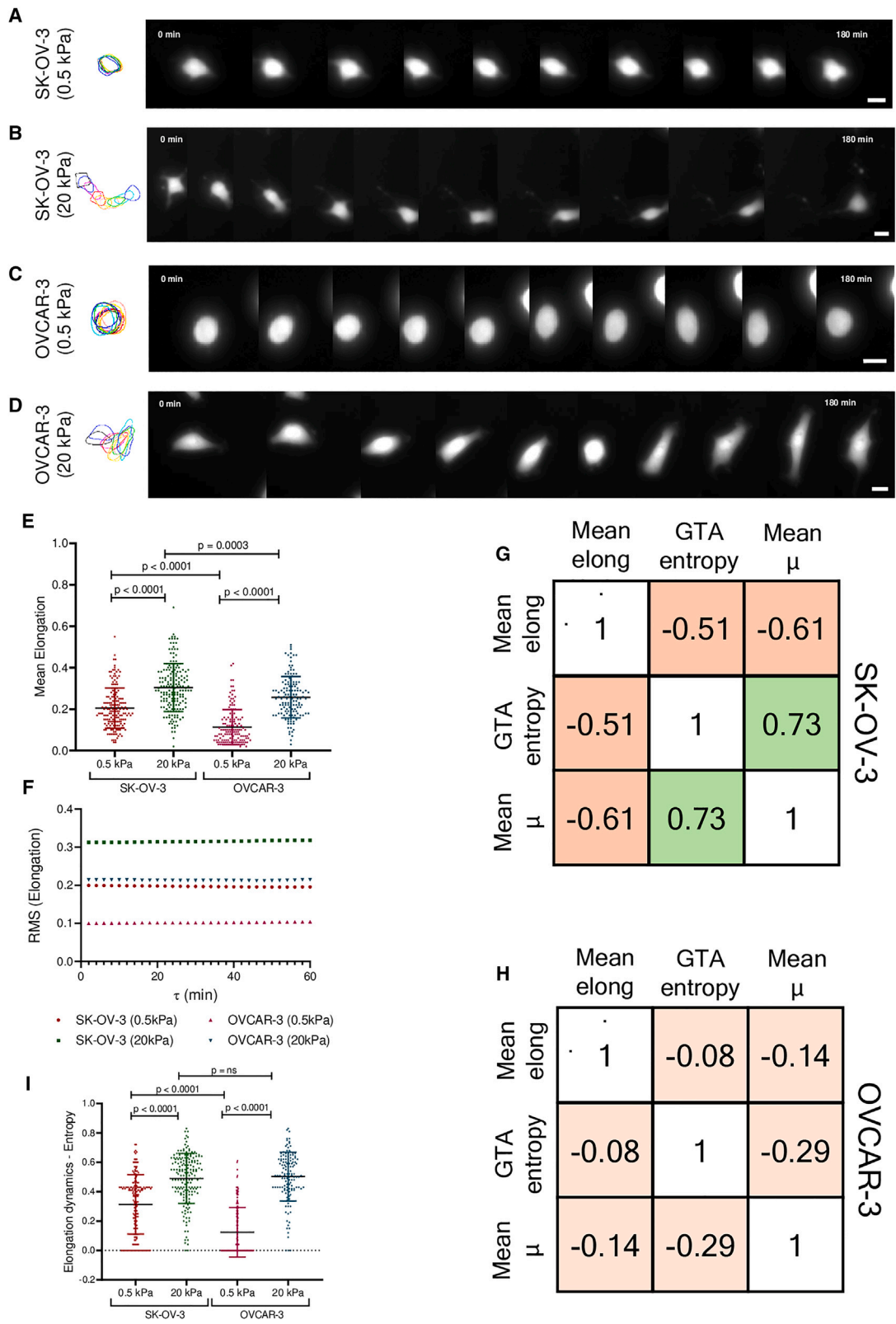
FIGURE 5 Determination of deformability dynamics in SK-OV-3 and OVCAR-3 cells. (*A–D*) Snapshots of time-lapse images at specific time points highlighting the change in the shape of cells over time (*A*, SK-OV-3 cells on 0.5 kPa; *B*, SK-OV-3 cells on 20 kPa; *C*, OVCAR-3 cells on 0.5 kPa; *D*, OVCAR-3 cells on 20 kPa) (representative snapshots for visualization are taken at time intervals of 20 min, however, the analysis is done for images acquired at 2-min intervals). (*E*) Comparative analysis of mean elongation values of both cell types on low and high stiffness. (*F*) Root mean-square of elongation values of a

(legend continued on next page)

their axis of polarization. In contrast, the mean elongation values of OVCAR-3 cells were poorly correlated with their GTA entropy (Fig. 5 H) (−0.08) and mean μ (−0.14) values, suggesting that the cellular cytoskeleton relieved such constraints on epithelioid cells to move in the direction of their shape polarization. In fact, whereas GTA entropy and mean μ for SK-OV-3 strongly correlated (0.73), they were mildly anticorrelated in OVCAR-3 cells, which can be explained by the slip behavior seen in these cells. Our results led us to examine the entropy of the elongation values: both cells also showed high entropic values for elongation dynamics on high stiffness compared with on softer substrata, as seen in Fig. 5 I (graph depicting mean entropy of elongation ratio of cells on soft and stiff substrata; statistical analysis is done using one-way ANOVA), indicating the significance of deformability for migration. Although, on stiffer environments, the entropy between the two cell types was insignificantly altered, the fold change in deformability for OVCAR-3 across stiffnesses was higher, suggesting that a more substrate-pliable cytoskeleton was driving its behavior of angular locomotion.

DISCUSSION

In this study, we propose a simple yet highly sensitive approach to capture the spatiotemporal dynamics of cell morphology and migration by combining mathematical imaging metrics and the concept of Shannon entropy. The metrics used here involve common descriptors, such as speed, turning angles, persistence ratio, and elongation, as well as recently developed metrics, such as major axis dynamics and morphomigrational angle. The number and combination of input variables, hence incorporated, allows us to build further on other elegant studies to infer data on cellular motility behavior. The study by Liu et al. showed entropic angular distribution as an indicator of cellular persistence, opening possibilities of utilizing information theory for understanding cellular migration (18). The current study uses a synergistic approach to further widen the interpretation scale of cellular plasticity in larger cell populations and across cellular motility trajectories (motivated by the future directions proposed at the end of the pioneering work by Kołodziej et al. (24)) and conditions with supportive numerical data. The constructed pipeline establishes the complex associations between the distinct morphogenetic metrics while reinforcing the interdependency between shape and motility dynamics in the context of microenvironmental cues (41). It also provides a wealth of data for the future construction of complex theoretical models of cellular motility.

In this study, ovarian cancer cells were found to be highly sensitive to biophysical cues from their microenvironment, resulting in distinct phenotypic behaviors. Tuning the stiffness of the underlying substratum, while keeping the ligand concentration and structure same, gave deeper insight into the effect of elastic regime of the substrata environment on cell deformability and motility. Current studies on understanding the role of substrata stiffness on cancer progression have looked majorly at static quantities, and are consistent with the fact that cells on higher stiffness have higher migratory capacity and spreading (42). Our analysis goes beyond this by showing that, compared with the directed persistent behavior of the mesenchymal SK-OV-3, the migratory mode of epithelioid OVCAR-3 cells on higher stiffness showed novel behaviors (Fig. 4). Epithelioid OVCAR-3 cells were in fact seen to surpass SK-OV-3 cells in their mean speed distribution on higher stiffness as well as exhibiting angular and slip motility, indicating a more exploratory behavior that would be possible on fibrosed tissues within the peritoneum. Our observations underscore the need to move beyond a conventional narrative of relative sessility and motility as shown by an epithelial and a mesenchymal cell type. Our findings also lead us to propose that cell speed may not be always correlated with the persistence of migration (43,44) (the correlation for SK-OV-3 comes to 0.42, whereas the faster but angular moving deformable OVCAR-3 cells show a correlation of 0.21). In this study, we chose the stiffness magnitudes of 0.5 and 20 kPa as they are representative of the elastic properties of untransformed (and stromal) and transformed tissues within the peritoneum, respectively. However, more extreme values (100 kPa and beyond) have also been reported, and future studies will examine motility behaviors on such substrata (38,39).

Recent studies have been investigating the interconvertibility of epithelial, mesenchymal, and ameboid cell states (8). Mesenchymal motility is known to be possible through filopodial or lamellipodial formation, where cell-matrix interaction plays a major role in the translocation of the cell. The mesenchymal cells are known to exert force on the matrix, which pushes the cell forward through actomyosin contractility. Ameboid cells, on the other hand, achieve much higher speed rates than mesenchymal cells by forming blebs, actin-rich pseudopodia, or highly contractile uropods. Their ability to "shape-shift" is attributed to constant reorganization of their actin cytoskeleton through rapid recycling (45). The ability of OVCAR-3 cells to show higher mean speed than mesenchymal SK-OV-3 suggests that OVCAR-3 cells might indeed display ameboid characteristics on higher stiffness. Recent investigations on the ability of cells to switch between different cellular states have indicated that

representative set shows time step invariance of elongation dynamics. (*G* and *H*) Correlation matrices between mean elongation values, mean entropy of GTA, and mean μ in SK-OV-3 (*G*) and OVCAR-3 (*H*) cells on high stiffness (*green shading* highlights correlation and *orange shading* highlights anticorrelation). (*I*) Comparative analysis on elongation entropy of both cell types at low and high stiffness (n = 3; statistical analysis was performed using one-way ANOVA). Scale bar, 20 μm. Videos S7, S8, S9, and S10 represent the time-lapse videos of the corresponding snapshots.

the ameboid state might lie within a larger spectra of state transitions in which epithelial and mesenchymal states reside (7,46). Furthermore, the ability of cells to reside in a hybrid state is consistent with the complexity and heterogeneity observed in cancer cell populations (47). In our study, the reduction in persistence ratio (Fig. 3 H) and increase in angular motion (Fig. 3, F and G) seen in OVCAR-3 cells at high stiffness, suggests that they might exhibit hybrid migrational behavior, as they lose their directionality but continue to move at higher speeds (Fig. 2 D). Representative snapshots of time-lapse images of OVCAR-3 cells on high stiffness (Figs. 3 D and 4 B) also show protrusion of fan-like lamellipodia during migration, which resembles actin polymerization-driven ameboid structures: we aim to investigate such cell biological phenomena in forthcoming papers (48). SK-OV-3 cells, on the other hand, are seen to show an elevated mesenchymal character with increased persistent directed motion on high stiffness.

Aberrant cell polarity signaling has also been known to be the leading cause of epithelial-to-mesenchymal transition, which in turn causes higher cancer invasiveness and metastasis (49). The loss in alignment of cellular polarity with respect to the direction of migration was also frequently seen in OVCAR-3 cells on high stiffness, where cells moved in a direction unrelated to the orientation of the cells. This loss in correlation, which we have referred to here as slip behavior, was seen to be a trait unique to OVCAR-3 cells (Fig. 4, B and F) and resulted in a constant change in their orientation as they underwent consistent tilting during angular motion on rigid gels. This was quantified and confirmed by high entropic values of Φ for OVCAR-3 cells in the same mechanical context (Fig. 4 C). Such hybrid behavior suggests that OVCAR-3, in general, might have higher mechanosensitivity and adaptive capacity to switch between different transition states, to increase its migratory and invasive potential. On the other hand, SK-OV-3 cells were found to have typical mesenchymal characteristics by forming lamellipodia or filopodia in the direction of motion, retaining cellular orientation in the direction of motion (Fig. 4, A and E). Stiffness was also seen to induce higher global deformability in both the cell types, indicating that morphodynamics and the microenvironment may cooperate to facilitate cells to attain their specific migratory mode (Fig. 5).

In summary, we demonstrate that a rigorous imaging approach combining morphology and migration metrics helps probe the spatiotemporal dynamics of the cellular phenotype, which can be extensively used to study pathological states such as cancer. In addition, it is seen that an interplay between the mechanical microenvironment and morphological traits produces distinct migratory modes in different ovarian cancer subtypes. While SK-OV-3 cells show elevated mesenchymal characteristics on high-stiffness gels, in the same environments OVCAR-3 cells show stunning diversity in migratory exploration and higher speed. In future studies, we will extend the study to a greater diversity of cell lines and microenvironmental contexts. In addition, we will investigate how these matrix-driven cues will modulate the dynamical phenotype of multicellular cancer collectives.

AUTHOR CONTRIBUTIONS

M.S. designed the experiments, executed the experiments, analyzed the results, and wrote the manuscript. R.B. conceived the project, designed the experiments, analyzed the results, and wrote the manuscript.

DECLARATION OF INTERESTS

The authors declare no competing interests.

SUPPORTING MATERIAL

Supporting material can be found online at https://doi.org/10.1016/j.bpj.2024.10.014.

REFERENCES

1. Bhat, R., B. Belardi, …, M. J. Bissell. 2016. Nuclear repartitioning of galectin-1 by an extracellular glycan switch regulates mammary morphogenesis. *Proc. Natl. Acad. Sci. USA.* 113:E4820–E4827.

2. Denning, D., and W. H. Roos. 2016. Elucidating the molecular mechanisms underlying cellular response to biophysical cues using synthetic biology approaches. *Cell Adhes. Migrat.* 10:540–553.

3. Friedl, P., and K. Wolf. 2010. Plasticity of cell migration: a multiscale tuning model. *J. Cell Biol.* 188:11–19.

4. Beunk, L., N. Wen, …, K. Wolf. 2023. Cell jamming in a collagen-based interface assay is tuned by collagen density and proteolysis. *J. Cell Sci.* 136:jcs260207.

5. Friedl, P., and K. Wolf. 2003. Tumour-cell invasion and migration: diversity and escape mechanisms. *Nat. Rev. Cancer.* 3:362–374.

6. Ribatti, D., R. Tamma, and T. Annese. 2020. Epithelial-Mesenchymal Transition in Cancer: A Historical Overview. *Transl. Oncol.* 13:100773.

7. Graziani, V., I. Rodriguez-Hernandez, …, V. Sanz-Moreno. 2022. The amoeboid state as part of the epithelial-to-mesenchymal transition programme. *Trends Cell Biol.* 32:228–242.

8. Alexandrova, A. Y., A. S. Chikina, and T. M. Svitkina. 2020. Actin cytoskeleton in mesenchymal-to-amoeboid transition of cancer cells. *Int. Rev. Cell Mol. Biol.* 356:197–256.

9. Elbez, R., J. Folz, …, R. Kopelman. 2021. Cell-morphodynamic phenotype classification with application to cancer metastasis using cell magnetorotation and machine-learning. *PLoS One.* 16:e0259462.

10. Mousavikhamene, Z., D. J. Sykora, …, N. Bagheri. 2021. Morphological features of single cells enable accurate automated classification of cancer from non-cancer cell lines. *Sci. Rep.* 11:24375.

11. Svensson, C. M., A. Medyukhina, …, M. T. Figge. 2018. Untangling cell tracks: Quantifying cell migration by time lapse image data analysis. *Cytometry A.* 93:357–370.

12. Yu, H., K. P. Lim, …, W. Shim. 2013. Functional Morphometric Analysis in Cellular Behaviors: Shape and Size Matter. *Adv. Healthcare Mater.* 2:1188–1197.

13. Sherwin, W. B., N. Prat I Fornells, and N. Fornells. 2019. The Introduction of Entropy and Information Methods to Ecology by Ramon Margalef. *Entropy.* 21:794.

14. Ameri, A. J., and Z. A. Lewis. 2021. Shannon entropy as a metric for conditional gene expression in Neurospora crassa. *G3 (Bethesda).* 11:jkab055.

15. van Wieringen, W. N., and A. W. van der Vaart. 2011. Statistical analysis of the cancer cell's molecular entropy using high-throughput data. *Bioinformatics.* 27:556–563.

16. Fuhrman, S., M. J. Cunningham, …, R. Somogyi. 2000. The application of Shannon entropy in the identification of putative drug targets. *Biosystems.* 55:5–14.

17. Liu, Y., Y. Jiao, …, L. Liu. 2021. Shannon entropy for time-varying persistence of cell migration. *Biophys. J.* 120:2552–2565.

18. Liu, Y., Y. Jiao, …, Z. Li. 2024. An entropy-based approach for assessing the directional persistence of cell migration. *Biophys. J.* 123:730–744.

19. Liu, Y., Y. Jiao, …, Z. Li. 2024. Morphological entropy encodes cellular migration strategies on multiple length scales. *NPJ Syst. Biol. Appl.* 10:26.

20. Eddy, C. Z., H. Raposo, …, B. Sun. 2021. Morphodynamics facilitate cancer cells to navigate 3D extracellular matrix. *Sci. Rep.* 11:20434.

21. Zhang, Z., L. Chen, …, E. Yoon. 2018. Morphology-based Prediction of Cancer Cell Migration Using an Artificial Neural Network and a Random Decision Forest. *Integr. Biol.* 10:758–767.

22. Song, T., Y. Choi, …, Y. K. Cho. 2023. A machine learning approach to discover migration modes and transition dynamics of heterogeneous dendritic cells. *Front. Immunol.* 14:1129600. https://doi.org/10.3389/fimmu.2023.1129600/full.

23. Conner, S., J. R. Guarin, …, M. J. Oudin. 2023. Cell morphology best predicts tumorigenicity and metastasis in vivo across multiple TNBC cell lines of different metastatic potential. Preprint at bioRxiv. https://doi.org/10.1101/2023.06.14.544969.

24. Kołodziej, T., A. Mielnicka, …, Z. Rajfur. 2023. Morphomigrational description as a new approach connecting cell's migration with its morphology. *Sci. Rep.* 13:11006.

25. Bray, F., M. Laversanne, …, A. Jemal. 2024. Global cancer statistics 2022: GLOBOCAN estimates of incidence and mortality worldwide for 36 cancers in 185 countries. *CA Cancer J. Clin.* 74:229–263.

26. Ciucci, A., M. Buttarelli, …, D. Gallo. 2022. Preclinical models of epithelial ovarian cancer: practical considerations and challenges for a meaningful application. *Cell. Mol. Life Sci.* 79:364.

27. Pickup, M. W., J. K. Mouw, and V. M. Weaver. 2014. The extracellular matrix modulates the hallmarks of cancer. *EMBO Rep.* 15:1243–1253.

28. Winkler, J., A. Abisoye-Ogunniyan, …, Z. Werb. 2020. Concepts of extracellular matrix remodelling in tumour progression and metastasis. *Nat. Commun.* 11:5120.

29. Deng, B., Z. Zhao, …, C. Zhou. 2022. Biological role of matrix stiffness in tumor growth and treatment. *J. Transl. Med.* 20:540.

30. Charras, G. T., M. Coughlin, …, L. Mahadevan. 2008. Life and Times of a Cellular Bleb. *Biophys. J.* 94:1836–1853.

31. Ryan, G. L., H. M. Petroccia, …, D. Vavylonis. 2012. Excitable Actin Dynamics in Lamellipodial Protrusion and Retraction. *Biophys. J.* 102:1493–1502.

32. Tse, J. R., and A. J. Engler. 2010. Preparation of Hydrogel Substrates with Tunable Mechanical Properties. *Curr. Protoc. Cell Biol.* 10:10.16–10.16.16.

33. Schindelin, J., I. Arganda-Carreras, …, A. Cardona. 2012. Fiji: an open-source platform for biological-image analysis. *Nat. Methods.* 9:676–682.

34. Sulewski, P. 2021. Equal-bin-width histogram versus equal-bin-count histogram. *J. Appl. Stat.* 48:2092–2111.

35. Shannon, C. E. 1948. A Mathematical Theory of Communication. *Bell System Technical Journal.* 27:379–423.

36. Uhlenbeck, G. E., and L. S. Ornstein. 1930. On the Theory of the Brownian Motion. *Phys. Rev.* 36:823–841.

37. Hu, Y., M. L. Becker, and R. K. Willits. 2023. Quantification of cell migration: metrics selection to model application. *Front. Cell Dev. Biol.* 11:1155882. https://doi.org/10.3389/fcell.2023.1155882.

38. Hopkins, T. I. R., V. L. Bemmer, …, I. E. Dunlop. 2021. Micromechanical mapping of the intact ovary interior reveals contrasting mechanical roles for follicles and stroma. *Biomaterials.* 277:121099.

39. Azzalini, E., N. Abdurakhmanova, …, S. Bonin. 2021. Cell-stiffness and morphological architectural patterns in clinical samples of high grade serous ovarian cancers. *Nanomedicine.* 37:102452.

40. Loosley, A. J., X. M. O'Brien, …, J. X. Tang. 2015. Describing Directional Cell Migration with a Characteristic Directionality Time. *PLoS One.* 10:e0127425.

41. Bhat, R., and M. J. Bissell. 2014. Of plasticity and specificity: dialectics of the microenvironment and macroenvironment and the organ phenotype. *WIREs Dev. Biol.* 3:147–163.

42. McKenzie, A. J., S. R. Hicks, …, A. K. Howe. 2018. The mechanical microenvironment regulates ovarian cancer cell morphology, migration, and spheroid disaggregation. *Sci. Rep.* 8:7228.

43. Maiuri, P., E. Terriac, …, M. Théry. 2012. The first World Cell Race. *Curr. Biol.* 22:R673–R675.

44. Maiuri, P., J. F. Rupprecht, …, R. Voituriez. 2015. Actin Flows Mediate a Universal Coupling between Cell Speed and Cell Persistence. *Cell.* 161:374–386.

45. Śliwa, A., A. Szczerba, …, A. Jankowska. 2024. A Recipe for Successful Metastasis: Transition and Migratory Modes of Ovarian Cancer Cells. *Cancers.* 16:783.

46. Liu, Y. J., M. Le Berre, …, M. Piel. 2015. Confinement and Low Adhesion Induce Fast Amoeboid Migration of Slow Mesenchymal Cells. *Cell.* 160:659–672.

47. Wu, J. S., J. Jiang, …, X. H. Liang. 2021. Plasticity of cancer cell invasion: Patterns and mechanisms. *Transl. Oncol.* 14:100899.

48. Schick, J., and E. Raz. 2022. Blebs—Formation, Regulation, Positioning, and Role in Amoeboid Cell Migration. *Front. Cell Dev. Biol.* 10:926394. https://doi.org/10.3389/fcell.2022.926394.

49. Gandalovičová, A., T. Vomastek, …, J. Brábek. 2016. Cell polarity signaling in the plasticity of cancer cell invasiveness. *Oncotarget.* 7:25022–25049.